https://doi.org/10.52131/jmps.2022.0302.0027

Journal of Materials and Physical Sciences

Volume 3, Number 2, 2022, Pages 59 - 70

Journal Homepage:
https://journals.internationalrasd.org/index.php/jmps

JOURNAL OF MATERIALS AND PHYSICAL SCIENCES
INTERNATIONAL RESEARCH ASSOCIATION FOR SUSTAINABLE DEVELOPMENT

Investigation of Dielectric, Magnetic and Electrical Behavior of BFO/GNPs Nano-Composites Synthesized via Sol-Gel Method

Arsa Nageena[1], Alina Manzoor[1*], Amir Muhammad Afzal[2], Muhammad Imran Arshad[1], Aamir Shahzad[1], Muhammad Kashif[1]

[1] Department of Physics, Government College University, Faisalabad,38000, Pakistan
[2] Department of Physics, Riphah International University, 13-Km Raiwind Road, Lahore-54000 Pakistan

ARTICLE INFO

Article History:
Received: August 08, 2022
Revised: September 13, 2022
Accepted: December 29, 2022
Available Online: December 31, 2022

Keywords:
Multiferroics $BiFeO_3$
XRD
Dielectric
Magnetization
Resistivity

ABSTRACT

Nano composites of $Ba_{0.5}Bi_{0.5}Nd_{0.05}Fe_{0.95}O_3$ multiferroic with graphene nano platelets $(GNPs)_x$ (x = 0, 0.125 %, 0.375 %, and 0.5 %) were synthesized using sol-gel auto ignition process. XRD analysis revealed a single rhombohedral distorted phase of $Ba_{0.5}Bi_{0.5}Nd_{0.05}Fe_{0.95}O_3$. The present study shows the impact of GNPs on the structural, electrical, dielectric, and magnetic properties of $Ba_{0.5}Bi_{0.5}Nd_{0.05}Fe_{0.95}O_3$ multiferroics. The substitution of Rare earth elements in pure BFO reduced the value of leakage current which is the basic drawback related with pure BFO. The prepared nanocomposites are then sintered at 800 °C for 7 hrs. The X-ray diffraction patterns showed the rhombohedral distorted perovskite crystal structure of the prepared samples including lattice constant, crystallite size, and X-ray density. The average crystallite sizes of the prepared nanocomposites are noticed in the range 28.14 -to 29.74 nm with increasing the GNPs concentration and lattice constant is found in the range 11.59 -to 11.61 Å. Temperature-dependent resistivity is first observed to increase with an increase in temperature then resistivity decreased with increasing the temperature which indicates a semi-conductor-like behavior as measured by two probe I-V characteristics. LCR technique showed that both the dielectric constant and the dissipation factor are decreased with an increase in frequency. VSM results indicated that saturation magnetization is noted to increase while remanent magnetization decreases with increasing concentration of GNPs.

*Corresponding Author's Email: alinamanzoor@hotmail.com

1. Introduction

In Multiferroic materials (BFO,) ferroelectricity and ferromagnetism coexist. In multiferroic ($BiFeO_3$) properties, electric and magnetic moderate to each other. Multiferroic materials are commonly studied due to wide range of spintronic device, sensor microelectronics device and information storage device.(Alina Manzoor et al., 2016; A Manzoor et al., 2015)

The crystal structure of bismuth multiferroic (BFO) is perovskite structure belongs to R3c space group with general formula ABO_3(Sobhan et al., 2015). Where A is a higher cation than B cation and O is oxygen. The main advantage of perovskite materials contains easy and simple fabrication, large solar adsorption, high flexibility of carriers for cell designs, less or low non-radiative charge carrier recombination and capitalization of dye-sensitive photovoltaic cells(Green, Ho-Baillie, & Snaith, 2014). Due to its multiferroic characteristics, bismuth ferrite (commonly known as $BiFeO_3$) has proven to be one of the most attractive perovskites. Bismuth ferrites $BiFeO_3$ are rhombohedral perovskites that belong to the R3c space group. Bismuth ferrites exhibit both ferromagnetic and ferroelectric properties at the same time. These structures have lattice parameters a_r = 5.63A°, a_r = 59.35 is a typical multiferroic, in which antiferromagnetic and ferroelectric exist simultaneously(Fatima, Ali, Iqbal, & Rizwan, 2017). Very important example BFO of a room temperature is a multiferroic materials with high range of Neel temperature T_N ~ 640 K and ferroelectric ordering with a Curie temperature Tc ~ 1103 K (A Manzoor et al., 2015; Tian et al., 2021). Bismuth ferrite is one of the most effective visible light-driven photo catalysts. Electrons move towards conduction bands when exposed to visible light, leaving holes in the valance band, which causes organic pollutants to degrade through oxidation and reduction processes. In perovskites structure the band gap can be changed by several methods for catalytic applications. Specifically, the band-gap in bismuth ferrites can be changed by doping with transition metals or (rare-earth elements) fabricating its composite structures with additional other materials such as graphene. Inside BFO co-substitution of iron and bismuth has been reported various times with increase magnetic, electric and photocatalytic properties. According to published research, rare-earth metal doping inside BFO significantly enhanced its physical and chemical properties(Kiani et al., 2019; Reetu, Agarwal, Sanghi, & Ashima, 2011; Umar et al., 2019).

Graphene is the two-dimensional crystalline form of carbon. Graphene contains a single layer of carbon atoms with remarkable properties, such as chemical and thermal stability, high electron mobility, excellent electrical conductivity, and large surface area(Akhavan, 2010). A high surface area is presented by single-layer of graphene. However it is exceedingly high cost and challenging to produce commercially. For environmental applications, graphene has exhibited good potential. Graphene and bismuth ferrites ($BiFeO_3$) combination creates an e-trapping medium that effectively separates electron-hole charge carriers, reduces recombination rates, and increases photocatalytic activity (An et al., 2013; Rostamnia, Doustkhah, Karimi, Amini, & Luque, 2015). Due to the high cost and difficulty of producing pristine graphene, graphene nanoplatelets (GNP), a cost-effective multilayer graphene product, has recently emerged as a strong option for several applications, including dye-sensitized supercapacitors solar cells, and others.

Graphene nanoplatelets (GNPs), are consist of multilayers of graphene in a range of 10 to 30 layers or more and a low-cost commercial product available in the form of flakes plates or particles. The GNPs are less susceptible to defects because of their nanometer-thickness. Excellent characteristics of GNPs include a efficient surface-to-volume ratio, low resistance, and strong mechanical qualities. Depending upon these characteristics the (GNPs) are very efficient materials usesd in photocatalysis, sensing, drug delivery, and optoelectronics device.

The majority of carbon-based $BiFeO_3$ composites used in photocatalytic processes are mainly depends on reduced graphene oxide or graphene. Mukherjee et al.(Mukherjee, Chakrabarty, Kumari, Su, & Basu, 2018) prepared $BiFeO_3$, along with reduced graphene oxide, is used for photocatalysis and water splitting. $BiFeO_3$ can be synthesized using a wide range of techniques, including the solid-state method, wet chemistry method, co-operation method, hydrothermal method, etc. Although the solid-state approach of synthesizing $BiFeO_3$ results in the pure phase of $BiFeO_3$ crystallites, there is typically poor uniformity and particle size control because of the high sintering temperature during the synthesis. Wet chemical approaches, including sol-gel and hydrothermal procedures, are therefore preferable because they produce higher homogeneity and allow for better control of particle size and purity of samples (Lam et al., 2021; Nkwachukwu & Arotiba, 2021; Remya et al., 2020). To enhance certain of its features, $BiFeO_3$ can be substituted with rare earth metal ion (Ma, Li, & Song, 2020; Waghmare et al., 2018; Zhang et al., 2012) and by adding graphene to prepare its composites to modify its dielectric and magnetic properties.

2. Experimental Procedure

In preparation of $Ba_{0.5}Bi_{0.5}Nd_{0.05}Fe_{0.95}O_3$ multiferroic the following metal nitrates including Barium Nitrate ($Ba(NO_3)_2$), Bismuth chloride ($BiCl_3$), Neodymium Nitrate Nano-hydrate ($Nd(NO_3)_3.H_2O$), iron nitrate ($Fe(NO_3)_3.9H_2O$), Citric Acid ($C_6H_8O_7$), and graphene nano-plates (GNPs)were used . For the preparation of the solution, deionized/

distilled water was used. GNPs doped $BiFeO_3$ ($Ba_{0.5}Bi_{0.5}Nd_{0.05}Fe_{0.95}O_3$) with four samples of doping using different compositions like (x = 0, 0.125 %, 0.375 % and 0.5 %) were synthesized by sol-gel route. Bismuth nitrate, barium chloride, Neodymium Nitrate Nano-hydrate, Iron Nitrate, Citric Acid and GNPs were dissolved into distilled water in beakers and then mixed in a specific measured quantity of distilled water in a 500ml sized beaker for further process. Obtained solutions of the samples were stirred with the help of a magnetic stirrer and for the sake of maintaining the pH of the samples at 7, the solution of Ammonia was added drop after drop into the solution. Different samples took different times for the conversion of a solution to be aqueous. Variation of time was in between 3 to 4 hours, and after further heat treatment for 25 minutes the solution was converted into Xero-gel, and ashes were seen in the beaker. Finally, after some time our required powder of nanocomposites was obtained. For mixing all the materials properly and to make the powder finer, this obtained powder of multiferroic was grinded for 30 minutes with the help of a mortar and pestle. After grinding, samples were managed in a furnace for the sintering process at 800°C for 7 hours. Sintering was done for condensing the materials. Regrinding was done for 40 minutes by using a mortar and pestle after sintering to make the fine powder of samples. The product was packed for further characterization.

To identify the required phase formation and crystal structure of the synthesized samples were identify by XRD diffractometer at room temperature in 20° -70° range. To determine the energy bandgap of under investigated samples UV-visible spectroscopy is employed. To confirm the dielectric response of materials in 1KHz-1MHz frequency range was observed with impedance analyzer. The M-H loops and magnetic properties of GNPs and Nd substituted bismuth ferrites were understand by VSM analysis. The electrical properties of $BFO/(GNPs)_x$ nanocomposites were study by using two probe IV measurements technique.

3. Results and Discussion

3.1. XRD Study

Figure 1 shows the XRD patterns of the $Ba_{0.5}Bi_{0.5}Nd_{0.05}Fe_{0.95}O_3/(GNPs)_x$ ferrites with GNPs concentration (x = 0, 0.125 %, 0.375 %, and 0.5 %) synthesized by the sol-gel method. Figure 1 demonstrated the XRD patterns of GNPs and Nd substituted the bismuth ferrites that confirmes the rhombohedral perovskite structure belongs to space group (R3c). It can be seen that typical peaks of multiferroic with six predominate peaks occurred at 2θ = 21.01°, 27.44°, 31.74°, 42.07°, 45.49° and 56.49° across miller indices or plane (012), (002), (104), (202), (024) and (300) respectively. These peaks indicate the development of the crystal structure. Along with the development of rhombohedral structures, also some traces of secondary phases were shaped. As can be seen, only a diffraction peak can be found in GNP pattern and is ascribed to the (002) plane. From the graph it is clear that when GNPs concentration rises the intensity of a some trends weak and becomes vanished (Rezlescu & Rezlescu, 1974). it is observed that there is no splitting of peaks. As concluded from the graph the most intense peak is (104), and the angle 2θ of the most intense peak is observed to be 31.74°. Average particle size of BiFeO3 is observed by the use of well known Scherrer equation(Bharati et al., 2020; Ishaque et al., 2016).

$$D = k\,\lambda / \beta \cos\theta \tag{1}$$

In above relation ß, D, λ, and K represent the wavelength of the X-ray, average crystallite size, peak broadening factor, and shape factors. It is observed that the value of 'D' enhanced by increasing the doping of GNPs. The cell volume and lattice constant (c and a) are calculated by using the equation.

$$V = a^2 c \times \sin 60^\circ \tag{2}$$

$$\frac{1}{d2} = \frac{4}{3}\frac{[h2 + hk + k2\,]}{a2} + \frac{l2}{c2} \tag{3}$$

Where h,k,l show the Millan indices. The "a" and "c" exhibit an upward-downward trend as substitution is increased. The X-ray density is calculated using the following equation.

$$\rho_x = \frac{8M}{V_{cell}N_A} \tag{4}$$

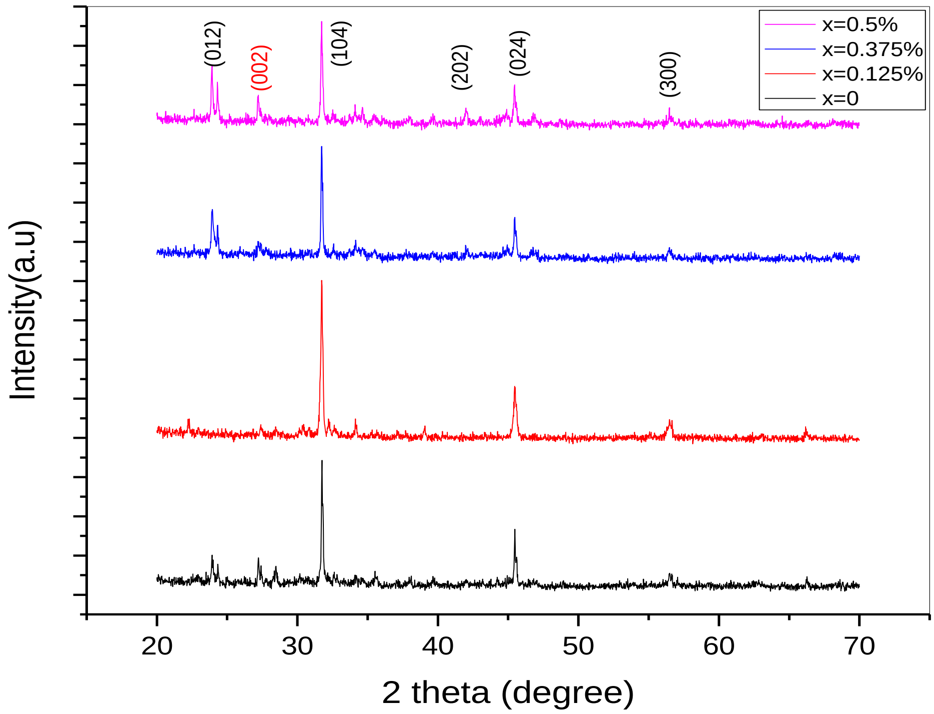

Figure 1: XRD patterns of BFO/GNP$_x$ nano composites (x=0.0, 0.125%, 0.375%, 0.5%)

Table 1

Crystallite size, X-ray density, Lattice constant (a and c), and unit cell volume of $Ba_{0.5}Bi_{0.5}Nd_{0.05}Fe_{0.95}O_3$ /(GNPs)$_x$ nano composites

(GNPs)$_x$ (X)	**Angle 2θ (degree)**	**Miller indices (hkl)**	**Crystallite size D (nm)**	**X-ray density (g/cm^3)**	**Lattice constant a (Å)**	**Unit cell volume V (Å)^3**
0	31.76°	(104)	36.19	7.06	5.63	376.62
0.125 %	31.73°	(104)	33.90	7.03	5.63	378.54
0.375 %	31.74°	(104)	34.97	7.02	5.634	378.97
0.5 %	31.74°	(104)	34.97	7.03	5.627	377.99

Here V_{cell}, M and N_A symbolizes the unit cell volume, molecular weight and Avogadro's number. Some other parameters like X-ray density, V_{cell} of bismuth ferrites (BFO) having hexagonal structure, bulk density, etc based on each composition are calculated and are listed below in Table 1. With increasing the doping of GNPs the value of x-ray density decreases in 7.02-7.06 g/cm^3 range and the value of V_{cell} increases 377.99-376.62 (Å)^3.. Scherer's formula is also used to determine the crystallite size (Patterson, 1939). The crystallite size is determined to be between 33.90- 36.19nm. which is significantly smaller than other reports on substituted ferrites nanoparticles. which have been reported to be between ~70 nm (Ahmadvand et al., 2010), 40-65 nm, and 36-58 nm. To obtain a suitable signal-to-noise ratio crystallite size play an important role in electronic devices and to achieve a good signal-to-noise ratio, crystallites must be less than 50 nm. The crystallite size in the present investigation is less than 50 nm, indicating that the synthesized materials may find use in the production of recording media devices to achieve the desired signal-to-noise ratio (Sultan et al., 2014).

3.2. Dielectric Properties

The room-temperature variation of dielectric constant (έ) and tangent loss (δ) for GNPs doped BFO nanocomposites for a frequency range of 4 Hz to 8 MHz are show in figures 2 & 3. The amount of electrostatic energy retained per unit volume per unit gradient is calculated by the dielectric constant. Through the substance of dielectric constant measured the speed of relative speed of electromagnetic signal which move in the substance. Dielectric constant was calculated using formula as;

$$\varepsilon' = \frac{Cp}{Co}, \qquad Co = \frac{A\epsilon o}{d} \qquad (5)$$

Where A is the area of pallet, Cp is parallel capacitance, ἑ is dielectric constant, d is thickness of pallet and ϵ_o is permittivity respectively. Figure 2 depicts the variation of dielectric constant (ἑ) as a function of applied field frequency. At the low frequency the dielectric constant exhibit the highest value which is due to impurities, moisture and dislocations. At high values of frequency, the values of the dielectric constant are so small that they become almost independent of the frequency.

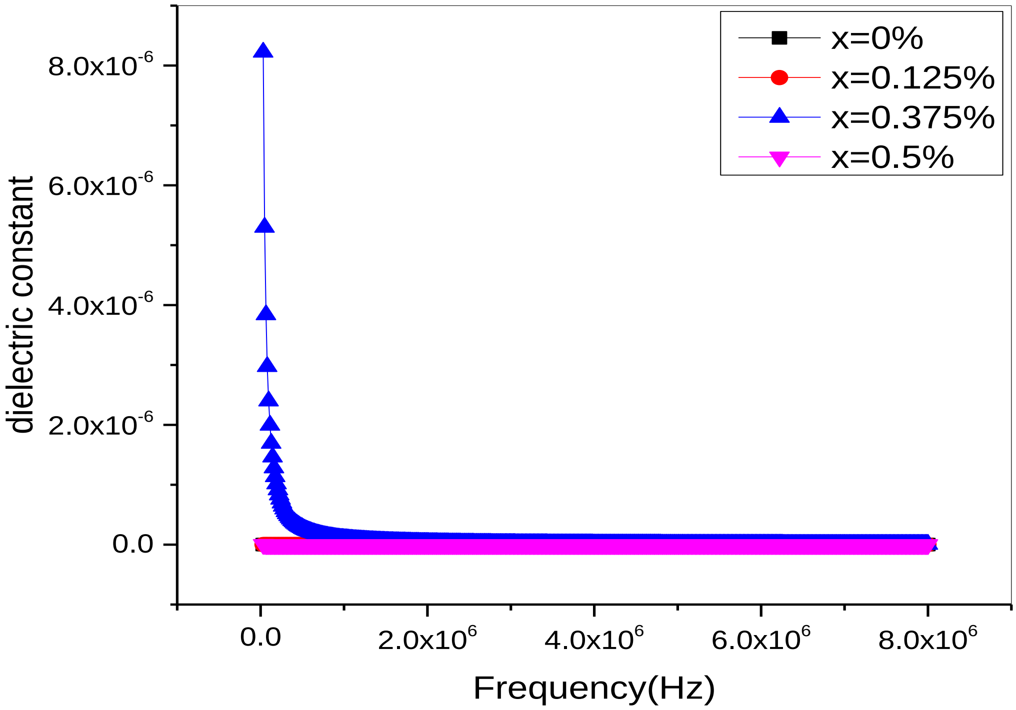

Figure 2: Frequency Vs permittivity of BFO/(GNPs)$_x$ nanocomposites

As the frequency increases the values of the dielectric constant become almost constant. In the starting low-frequency, range dielectric constant have higher values are explain on the basis of the space charge polarization due to in homogeneous present in dielectric structure (Kumar & Yadav, 2011). The dielectric constant follows the applied frequency in the low region frequency region up to 1 MHz after that graph merge each other and shows the independent behavior up to 8 MHz for all compositions. The highest value of dielectric constant is obtained at x = 0.375 % as compared to all other samples. It is concluded that the contribution of electrons to measure the dielectric parameters is independent of applied field frequency (Dai, Chen, Li, Xue, & Chen, 2013). On both sides, when ions equally the applied frequency and natural frequency of field becomes almost equal, power loss rises and resonance peak take place (Khan et al., 2016). $Ba_{0.5}Bi_{0.5}Nd_{0.05}Fe_{0.95}O_3$/(GNPs)$_x$ composites consist of conducting grains separated by high resistive grain boundaries understood by Koop's theory and Maxwell-Wagner model of dielectrics (Ali, Islam, Awan, & Ahmad, 2013; Dilshad et al., 2016; Shaikh et al., 2021).

Dielectric tangent loss is given by:

$$\mathrm{Tan}\delta = \frac{1}{2\pi f CpRp} \qquad (6)$$

C_p is parallel capacitance, f is frequency and R_p is the parallel resistance, respectively. Baviour of tangent loss for $Ba_{0.5}Bi_{0.5}Nd_{0.05}Fe_{0.95}O_3/(GNPs)_x$ composites with respect to frequency at room temperature is shown in figure 3.

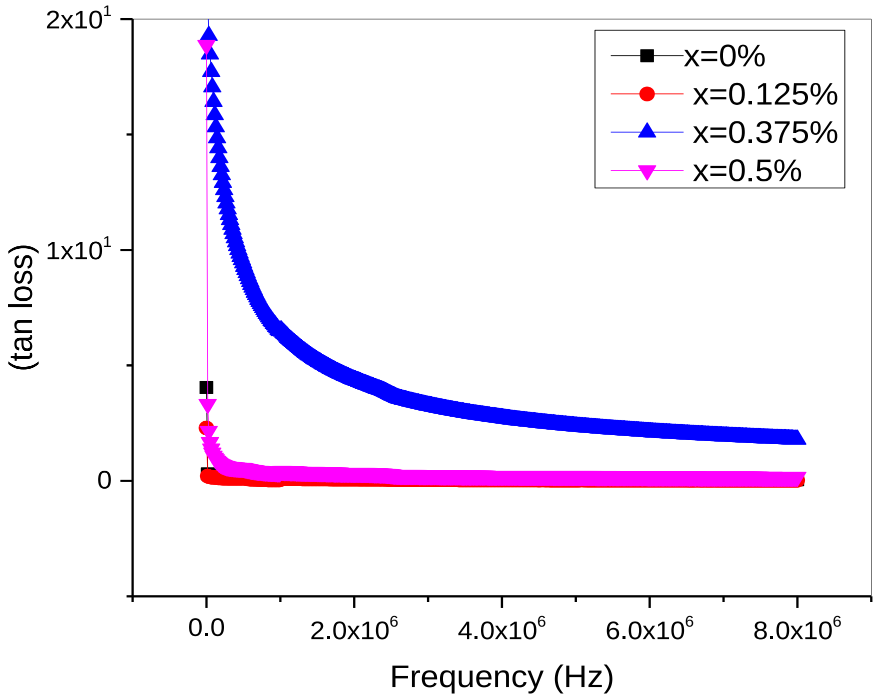

Figure 3: Frequency vs tangent loss of BFO/$(GNPs)_x$ nanocomposites

Figure 3 depicts the variation of dielectric loss of BFO/$(GNPs)_x$ nanocomposites follow the applied frequency. In the low frequency region dielectric loss decreases due to the involvement of grains. At high frequency region of 2MHz-8 MHz the dielectric loss exhibit frequency independent behavior because the dipoles are aligned in the direction of applied frequency. From the graph it is clear that the maximum value of tangent loss is observed for x= 0.375 % sample as compared to all other samples. The loss are strongly dependent on some other important factors including oxygen vacancies, interfacial polarization and predomenently on applied frequency. (Chen, J. *et al.,* (2013). Dielecric dispersion in ferrites is based on Koop's phenomenological theory and Maxwell-Wagner's model. Tangent loss in ferrites is considered to be creating from two phenomena: charged defect dipoles and hopping of electrons.

3.3. Impedance Spectroscopy

Standard impedance spectroscopy was used to investigate the electrical properties of the samples and was carefully examined in terms of interfacial/electrode, grain, grain boundary, etc. Impedance technique was used to record electrical responses at particular temperatures when a sinusoidal signal with a frequency of 1 KHz to 8 MHz was applied (Brahma et al., 2022). The change in the impedance with respect to the frequency is shown in the figure. As the frequency increase, the measured value of impedance decreases. With the increasing frequency values, the impedance decreases, and at a point, the value of impedance almost becomes constant and seems to be independent of the frequency due to the space charge polarization caused by the accumulation/increase of carriers, including polarons, vacancies, and defects in the ceramics energetic by the high frequency, which leads to the maximum conductivity (priyadarsini Jena, Mohanty, Parida, Parida, & Nayak, 2020). For concentration x=0.375 % there is constant with increasing frequency.

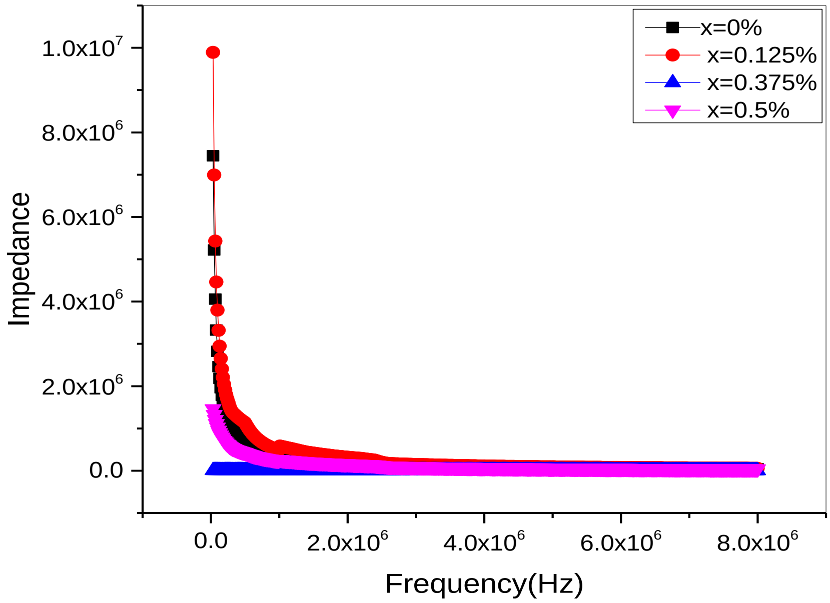

Figure 4: Frequency vs Impedance of BFO/(GNPs)$_x$ nanocomposites

3.4. Electrical Resistivity

The log resistivity (ρ) versus 1000/T, also called Arrhenius plots are shown in figure 5. Current-Voltage(I-V) measurements are taken to measure the conducting capacity of the prepared photocatalysts. With the application of applied voltage (− 4.5 V to +4.5 V) the response of current was calculated. hydraulic press was utilized to make a pellet of definite dimensions. The conductivity and resistivity of all prepared sample were calculated by using this formula:

$$\rho = \frac{RA}{h} \tag{7}$$

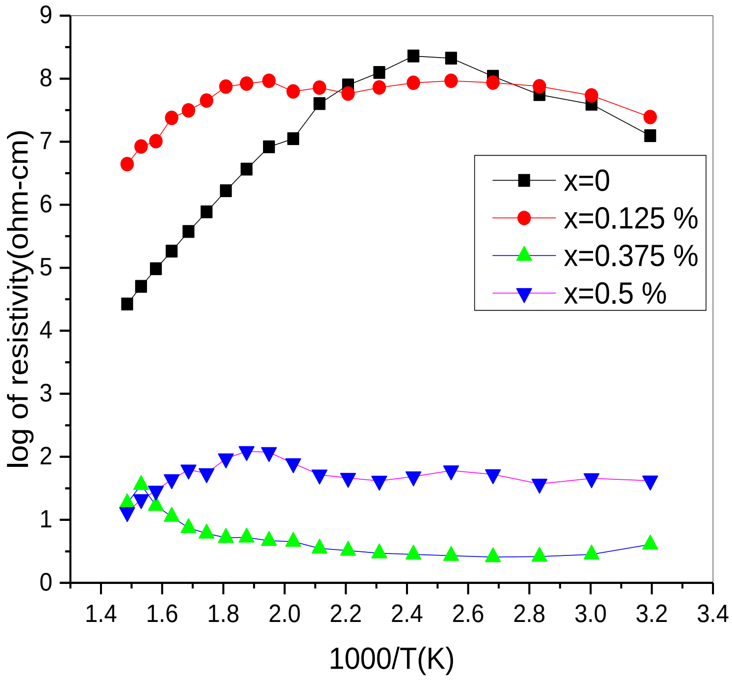

Figure 5: Arrhenius plots of BFO/(GNPs)$_x$ nanocomposites

Where ρ, R, A, and h represented resistivity, resistance, area of pallet and thickness of the pallet, respectively. The resistance is calculated using ohms law (V = IR). In this research work, it is excluded that in the material the log resistivity is decreased and then decreased which manipulates the conductor and semiconductor behavior. In the start at the lower temperature values, the fabricated material showed the behavior of conductor but as the temperature increased the value of resistivity decreased which showed the semiconductor behavior of the fabricated material. So, in this research work, it is observed that the BFO/$(GNPs)_x$ nanocomposites have both conductor and semiconductor behavior at the prescribed compositions and this behavior totally depends on the temperature. By changing the temperature, the behavior of the fabricated material also changed. I–V graphs for all under investigated photocatalyst materials are shown in Fig. 5. The calculated values of electrical conductivity (σ) for all $BiFeO_3$, Gd-doped $BiFeO_3$, and Gd-doped $BiFeO_3$/rGO nanocomposite were 3.61×10^{-14} S/cm, 3.02×10^{-13} S/cm, and 0.12×10^{-9} S/cm, respectively.

3.5. UV-Visible Spectroscopy Analysis

UV-visible spectroscopy is used for the study of optical properties of BFO/$(GNPs)_x$ as shown in figure 6. Figure 6 has shown the optical absorbance of BFO/$(GNPs)_x$ nanocomposites in the range of 200-800 nm. Initially, optical absorption is high and after that with increasing the concentrartion of wavelength, it decreased. It is observed that variation in peak such as absorbance varies with the variation of wavelength. To calculate the band gap (E_g), the given below relation is used:

$$\alpha h\nu = A(h\nu - E_g)^n \quad (8)$$

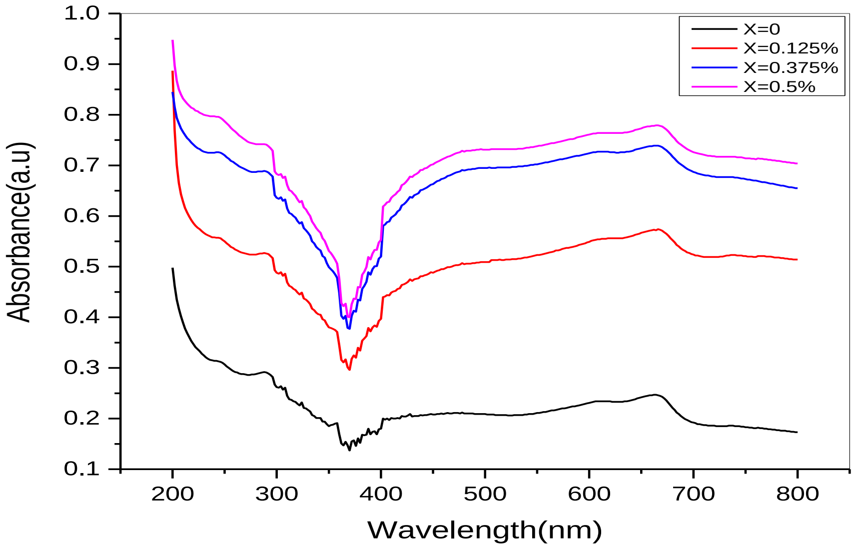

Figure 6: Absorbance vs Wavelength of BFO/$(GNPs)_x$ nanocomposites

Here *α*, *hv*, A, n, and E_g are absorption coefficient, photon energy, integer, and band gap energy respectively. The E_g is calculated using n for allowed direction transition. The calculated values of E_g from experimental data are 2.71 eV, 2.79 eV, 2.85 eV, and 2.88 eV for samples $(GNPs)_0$, $(GNPs)_{0.125\%}$, $(GNPs)_{0.375\%}$, and $(GNPs)_{0.5\%}$, respectively as shown in figure 7. In this experiment it is note that band gap continuously increases and turned toward lies in visible region with increasing the concentration of GNPs. This variation in band gap is directly depend on GNPs concentration and phenomenon is mainly due to the hybridization between CFO and GNPs nanostructures. This increase in hybridization between CFO and GNPs is due to the strong Fe–O–C bonds. The additional energy levels that are introduced by this chemical interaction between the composite material's conduction and valence bands, band gap energy is reduced (Devi & Srinivas, 2017). Conversely, it is observed that, increase the concentration of GNPs band gap increase. This difference for higher doping of GNPs was mainly by Burstein-Moss effect. By the application of this effect in semiconductor materials the conduction band is full of electrons. So maximum number of electrons enter in conduction band from the grapheme. As a result higher concentration of GNPs provide more π-electrons to transfer the conduction band of CFO nanostructures(Israr et al., 2020).

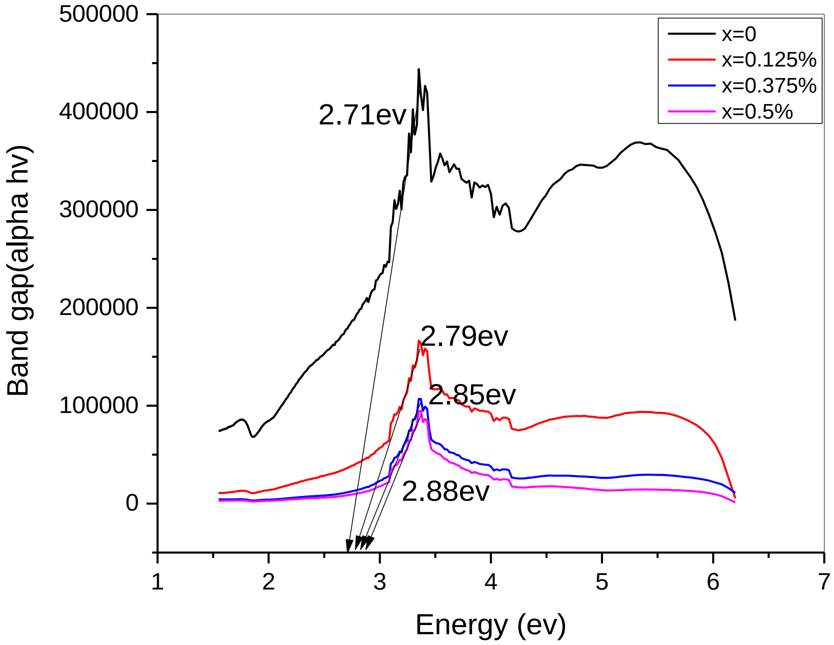

Figure 7: Energy vs bandgap of BFO/(GNPs)ₓ nanocomposites

3.6. Magnetic Analysis

The magnetic behavior of GNPs doped $Ba_{0.5}Bi_{0.5}Nd_{0.05}Fe_{0.95}O_3$ nanocomposites is investigated using vibrating sample magnetometer at room temperature. The M-H loops of all prepared nanocomposites are shown in figure 8. The magnetic parameters of the synthesized samples, such as remanence (Mr), saturation magnetization (Ms), and coercivity (Hc) are determined from M - H loops and are listed in Table 2. Due to the high value of leakage current and coercivity all the M-H loops are broken and unsaturated (Ahmed et al., 2022). So, to produce M-H loops for BFO, the higher applied voltage is not favorable as under observation samples are damaged under high temperatures. As can be seen from Table 2, the saturation magnetization is decreased from 35.95 -to 27.18 emu/g and the value of remanence magnetization (Mr) is increased from 6.59 -to 11.27 emu/g up to substitution level x=0 to 0.125 % of GNPs. After this, the value of Ms is increased from 27.18 -to 36.89 emu/g whereas the remanent magnetization is decreased from substitutional level x= 0.125 % to 0.5 % with an increase in the GNPs concentration. With GNPs doping, the highest value of saturation magnetization is 36.89 emu/g for substitution level x=0.5 % and highest value of remanent magnetization is 11.27 emu/g for x= 0.125 %. The coercivity first decreases from 168.75 to 130.43 Oe for x= 0 to 0.125 % then it increases suddenly with an increase in the concentration of GNPs. The nano composites of $Bi_{0.5}Ba_{0.5}Nd_{0.05}Fe_{0.95}O_3$ and GNPs have a significant impact on their magnetic properties.

Table 2
Magnetic parameters such as saturation magnetization (Ms), remanence magnetization (Mr), coercivity (Hc) and ratio $\frac{Mr}{Ms}$ from hysteresis loops of BFO/(GNPs)ₓ nanocomposites

Concentrations (GNPs)ₓ	Ms (emu/g)	Mr (emu/g)	Hc (Oe)	Remanent ratio (emu/g) R= Mr/Ms
0	35.95	6.59	168.75	0.18
0.125 %	27.18	11.27	130.43	0.41
0.375 %	29.48	3.75	149.99	0.13
0.5 %	36.89	3.64	160.27	0.098

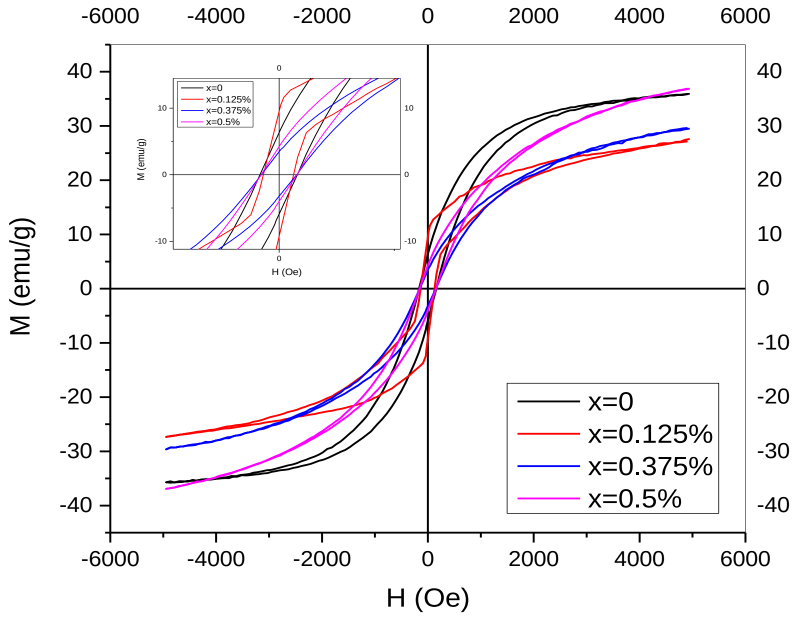

Figure 8: Combined MH loops of BFO/(GNPs)$_x$ nanocomposites

Conclusion

GNPs doped BFO multiferroics were successfully prepared by self- ignited auto combustion sol-gel method. XRD patterns showed that BFO/GNPs nano composites possessed a rhombohedral distorted perovskite structure. Crystallite size was found below 50 nm while lattice constant was noted in the range of 5.62-5.63 Å. Dielectric constant and dissipation factor were observed to decrease with an increase in frequency. Electrical properties revealed the semiconductor type behavior of BFO/GNPs nano composites. UV-visible spectroscopy analysis showed that band gap rises with higher GNPs ratio due to Burstein-Moss effect would permit more π-electrons to enter the conduction band. The saturation magnetization increased while remnant magnetization decreased with increasing concentration of GNPs.

The importance of iron is well-known, and it is being employed in various engineering applications due to superior mechanical properties, appropriate corrosion resistance at a wide range of pH, and availability at a cheaper cost(McNeill & Edwards, 2001; Nishikata, Ichihara, Hayashi, & Tsuru, 1997). Although the use of pure iron is limited due to stability issues because some applications demand extended stability and lesser density to strength ratio. Therefore, iron has been replaced by other materials like aluminum, magnesium, stainless steel, and other alloys in various fields of applications. But this material is still being used in many applications and the material scientists have always been working to counter its associated problems and to improve its properties for various applications.

References

Ahmadvand, H., Salamati, H., Kameli, P., Poddar, A., Acet, M., & Zakeri, K. (2010). Exchange bias in LaFeO3 nanoparticles. *Journal of Physics D: Applied Physics, 43*(24), 245002.

Ahmed, I., Mustafa, G., Subhani, M. U., Hussain, G., Ismail, A. G., & Anwar, H. (2022). A detailed investigation of lanthanum substituted bismuth ferrite for enhanced structural, optical, dielectric, magnetic and ferroelectric properties. *Results in Physics, 38*, 105584.

Akhavan, O. (2010). Graphene nanomesh by ZnO nanorod photocatalysts. *ACS nano, 4*(7), 4174-4180.

Ali, I., Islam, M., Awan, M., & Ahmad, M. (2013). Effects of heat-treatment time on the structural, dielectric, electrical, and magnetic properties of BaM hexaferrite. *Journal of materials engineering and performance, 22*(7), 2104-2114.

An, J., Zhu, L., Wang, N., Song, Z., Yang, Z., Du, D., & Tang, H. (2013). Photo-Fenton like degradation of tetrabromobisphenol A with grapheneBiFeO3 composite as a catalyst. *Chemical engineering journal, 219*, 225-237.

Bharati, V., Somvanshi, S. B., Humbe, A. V., Murumkar, V., Sondur, V., & Jadhav, K. (2020). Influence of trivalent Al–Cr co-substitution on the structural, morphological and Mössbauer properties of nickel ferrite nanoparticles. *Journal of Alloys and Compounds, 821*, 153501.

Brahma, F., Sahoo, L., Bhattacharjee, S., Hota, R., Parida, B., & Parida, R. (2022). Investigation of impedance and leakage feature in BFO-BTO perovskite system. *Materials Today: Proceedings, 67*, 1175-1179.

Dai, H., Chen, Z., Li, T., Xue, R., & Chen, J. (2013). Structural and electrical properties of bismuth ferrite ceramics sintered in different atmospheres. *Journal of superconductivity and novel magnetism, 26*(10), 3125-3132.

Devi, L. G., & Srinivas, M. (2017). Hydrothermal synthesis of reduced graphene oxide-CoFe2O4 heteroarchitecture for high visible light photocatalytic activity: Exploration of efficiency, stability and mechanistic pathways. *Journal of environmental chemical engineering, 5*(4), 3243-3255.

Dilshad, M., Nazim, S., Warsi, M. F., Shahid, M., Naseem, S., Riaz, S., . . . Khan, M. A. (2016). Fabrication and characterization of Ni1+ x ZrxFe2− 2xO4 nanoparticles for potential applications in high frequency devices. *Ceramics International, 42*(14), 16359-16363.

Fatima, S., Ali, S. I., Iqbal, M. Z., & Rizwan, S. (2017). The high photocatalytic activity and reduced band gap energy of La and Mn co-doped BiFeO 3/graphene nanoplatelet (GNP) nanohybrids. *RSC advances, 7*(57), 35928-35937.

Green, M. A., Ho-Baillie, A., & Snaith, H. J. (2014). The emergence of perovskite solar cells. *Nature photonics, 8*(7), 506-514.

Ishaque, M., Khan, M. A., Ali, I., Athair, M., Khan, H. M., Iqbal, M. A., . . . Warsi, M. F. (2016). Synthesis of nickel–zinc–yttrium ferrites: Structural elucidation and dielectric behavior evaluation. *Materials Science in Semiconductor Processing, 41*, 508-512.

Israr, M., Iqbal, J., Arshad, A., Rani, M., Gómez-Romero, P., & Benages, R. (2020). Graphene triggered enhancement in visible-light active photocatalysis as well as in energy storage capacity of (CFO) 1-x (GNPs) x nanocomposites. *Ceramics International, 46*(3), 2630-2639.

Khan, H. M., Islam, M., Xu, Y., Ali, I., Asif Iqbal, M., Ishaque, M., . . . Sadiq, I. (2016). Electrical transport properties and temperature-dependent magnetization behavior of TbZn-substituted Ca0. 5Ba0. 5Fe12O19 hexaferrites. *Journal of Sol-Gel Science and Technology, 78*(1), 151-158.

Kiani, M., Kiani, A. B., Khan, S. A., ur Rehmana, S., Khan, Q. U., Mahmood, I., . . . Zhu, L. (2019). Facile synthesis of Gd and Sn co-doped BiFeO3 supported on nitrogen doped graphene for enhanced photocatalytic activity. *Journal of Physics and Chemistry of Solids, 130*, 222-229.

Kumar, A., & Yadav, K. (2011). A systematic study on magnetic, dielectric and magnetocapacitance properties of Ni doped bismuth ferrite. *Journal of Physics and Chemistry of Solids, 72*(11), 1189-1194.

Lam, S.-M., Jaffari, Z. H., Sin, J.-C., Zeng, H., Lin, H., Li, H., & Mohamed, A. R. (2021). Insight into the influence of noble metal decorated on BiFeO3 for 2, 4-dichlorophenol and real herbicide wastewater treatment under visible light. *Colloids and Surfaces A: Physicochemical and Engineering Aspects, 614*, 126138.

Ma, C.-J., Li, N., & Song, W.-L. (2020). Tailoring the electrochemical behaviors of bismuth ferrite using Ca ion doping. *Frontiers in Materials, 7*, 15.

Manzoor, A., Afzal, A., Amin, N., Arshad, M. I., Usman, M., Rasool, M., & Khan, M. (2016). Investigation of dielectric and optical properties of structurally modified bismuth ferrite nanomaterials. *Ceramics International, 42*(9), 11447-11452.

Manzoor, A., Afzal, A., Umair, M., Ali, A., Rizwan, M., & Yaqoob, M. (2015). Synthesis and characterization of Bismuth ferrite (BiFeO3) nanoparticles by solution evaporation method. *Journal of Magnetism and Magnetic Materials, 393*, 269-272.

McNeill, L. S., & Edwards, M. (2001). IRON PIPE corrosion IN DISTRIBUTION SYSTEMS. *Journal - American Water Works Association, 93*(7), 88-100. doi:10.1002/j.1551-8833.2001.tb09246.x

Mukherjee, A., Chakrabarty, S., Kumari, N., Su, W.-N., & Basu, S. (2018). Visible-light-mediated electrocatalytic activity in reduced graphene oxide-supported bismuth ferrite. *Acs Omega, 3*(6), 5946-5957.

Nishikata, A., Ichihara, Y., Hayashi, Y., & Tsuru, T. (1997). Influence of Electrolyte Layer Thickness and pH on the Initial Stage of the Atmospheric Corrosion of Iron. *Journal of The Electrochemical Society, 144*(4), 1244-1252. doi:10.1149/1.1837578

Nkwachukwu, O. V., & Arotiba, O. A. (2021). Perovskite oxide–based materials for photocatalytic and photoelectrocatalytic treatment of water. *Frontiers in Chemistry*, 142.

Patterson, A. (1939). The Scherrer formula for X-ray particle size determination. *Physical review, 56*(10), 978.

priyadarsini Jena, D., Mohanty, B., Parida, R., Parida, B., & Nayak, N. C. (2020). Dielectric and thermal behavior of 0.75 BiFeO3-0.25 BaTiO3 filled ethylene vinyl acetate composites. *Materials Chemistry and Physics, 243*, 122527.

Reetu, Agarwal, A., Sanghi, S., & Ashima. (2011). Rietveld analysis, dielectric and magnetic properties of Sr and Ti codoped BiFeO3 multiferroic. *Journal Of Applied Physics, 110*(7), 073909.

Remya, K., Prabhu, D., Joseyphus, R. J., Bose, A. C., Viswanathan, C., & Ponpandian, N. (2020). Tailoring the morphology and size of perovskite BiFeO3 nanostructures for enhanced magnetic and electrical properties. *Materials & Design, 192*, 108694.

Rezlescu, N., & Rezlescu, E. (1974). Dielectric properties of copper containing ferrites. *physica status solidi (a), 23*(2), 575-582.

Rostamnia, S., Doustkhah, E., Karimi, Z., Amini, S., & Luque, R. (2015). Surfactant-Exfoliated Highly Dispersive Pd-Supported Graphene Oxide Nanocomposite as a Catalyst for Aerobic Aqueous Oxidations of Alcohols. *ChemCatChem, 7*(11), 1678-1683.

Shaikh, B. R., Toksha, B. G., Shirsath, S. E., Chatterjee, A., Tonde, S., & Chishty, S. Q. (2021). Microstructure, magnetic, and dielectric interplay in NiCuZn ferrite with rare earth doping for magneto-dielectric applications. *Journal of Magnetism and Magnetic Materials, 537*, 168229.

Sobhan, M., Xu, Q., Zhao, J., Franklin, A., Hu, Y., Tse, J., & Wu, P. (2015). Modification of surface chemistry by lattice Sn doping in BiFeO3 nanofibers. *EPL (Europhysics Letters), 111*(1), 18005.

Sultan, A., Mahmood, A., Goraya, N. K., Qureshi, A. M., Ahmad, I., Ashiq, M. N., . . . Warsi, M. F. (2014). New nanoparticulate Gd1− xZrxFe1− yMnyO3 multiferroics: Synthesis, characterization and evaluation of electrical, dielectric and magnetic parameters. *Journal of Alloys and Compounds, 585*, 790-794.

Tian, Y., Xue, F., Tang, L., Li, W., Jing, L., & Li, S. (2021). Structural, impedance spectrum, and physical properties of Gd and Ti co-doped BiFeO3 ceramics synthesized by spark plasma sintering. *Journal of Materials Science: Materials in Electronics, 32*(14), 18825-18836.

Umar, M., Mahmood, N., Awan, S. U., Fatima, S., Mahmood, A., & Rizwan, S. (2019). Rationally designed La and Se co-doped bismuth ferrites with controlled bandgap for visible light photocatalysis. *RSC advances, 9*(30), 17148-17156.

Waghmare, S. D., Jadhav, V. V., Shaikh, S. F., Mane, R. S., Rhee, J. H., & O'Dwyer, C. (2018). Sprayed tungsten-doped and undoped bismuth ferrite nanostructured films for reducing and oxidizing gas sensor applications. *Sensors and Actuators A: Physical, 271*, 37-43.

Zhang, Z., Liu, H., Lin, Y., Wei, Y., Nan, C.-W., & Deng, X. (2012). Influence of La doping on magnetic and optical properties of bismuth ferrite nanofibers. *Journal of Nanomaterials, 2012*.